Journal of Magnetic Resonance 303 (2019) 1–6

Contents lists available at ScienceDirect

Journal of Magnetic Resonance

journal homepage: www.elsevier.com/locate/jmr

Four millimeter spherical rotors spinning at 28 kHz with double-saddle coils for cross polarization NMR

Chukun Gao [a], Patrick T. Judge [a,b], Erika L. Sesti [a], Lauren E. Price [a], Nicholas Alaniva [a], Edward P. Saliba [a], Brice J. Albert [a], Nathan J. Soper [a], Pin-Hui Chen [a,c], Alexander B. Barnes [a,*]

[a] Department of Chemistry, Washington University in St. Louis, St. Louis, MO 63130, USA
[b] Department of Biochemistry, Biophysics & Structural Biology, Washington University in St. Louis, St. Louis, MO 63110, USA
[c] Department of Physics, Washington University in St. Louis, St. Louis, MO 63130, USA

ARTICLE INFO

Article history:
Received 31 January 2019
Revised 7 March 2019
Accepted 20 March 2019
Available online 1 April 2019

Keywords:
MAS spheres, cross polarization
Dynamic nuclear polarization
Magic angle spinning
Nuclear magnetic resonance
Spherical rotors

ABSTRACT

Spherical rotors in magic angle spinning (MAS) experiments have significant advantages over traditional cylindrical rotors including simplified spinning implementation, easy sample exchange, more efficient microwave coupling for dynamic nuclear polarization (DNP), and feasibility of downscaling to access higher spinning frequencies. Here, we implement spherical rotors with 4 mm outside diameter (o.d.) and demonstrate spinning >28 kHz using a single aperture for spinning gas. We show a modified stator geometry to improve fiber optic detection, increase NMR filling factor, and improve alignment for sample exchange and microwave irradiation. Higher NMR Rabi frequencies were obtained using smaller radiofrequency (RF) coils on small-diameter spherical rotors, compared to our previous implementation of MAS spheres with an o.d. of 9.5 mm. We report nutation fields of 110 kHz on ^{13}C with 820 W of input power and 100 kHz on ^{1}H with 800 W of input power. Proton decoupling fields of 78 kHz were applied over 20 ms of signal acquisition without any sign of arcing. Compared to our initial demonstration of a split coil for 9.5 mm spheres, this current implementation of a double-saddle coil inductor for 4 mm spheres not only intensifies the RF fields, but also improves RF homogeneity. We achieve an 810°/90° nutation intensity ratio of 0.84 at 300.197 MHz (^{1}H). We also show electromagnetic simulations predicting a nearly 3-fold improvement in electron Rabi frequency of 0.99 MHz (with 4 mm spheres) compared to 0.38 MHz (with 3.2 mm cylinders), with 5 W of incident microwave power. Further improvements in magnetic resonance spin control are expected as RF inductors and microwave coupling are optimized for spherical rotors and scaled down to the micron scale.

1. Introduction

Nuclear magnetic resonance (NMR) spectroscopy is unique in its ability to probe molecular structure and dynamics of liquids and solids with atomic resolution, making it an important and versatile analytical method. In solids, magic angle spinning (MAS) significantly improves NMR resolution by partially averaging anisotropic spin interactions [1–4]. MAS NMR experiments require mechanical sample rotation along an axis of 54.7° with respect to the static magnetic field [5,6]. MAS has enhanced the applicability of solid-state NMR to a wide variety of chemical environments and molecular architectures including crystalline proteins [7–11], membrane proteins [12–22], amyloid fibrils [23–26], cell walls [27–33], and materials [34–38].

Samples are usually packed into hollow cylindrical rotors in conventional MAS. This geometry requires bearing gas to suspend the rotor with minimal friction, and drive gas to generate spin propulsion. However, wobbling of cylinders about the long axis can cause collisions that destroy the sample and rotor. Further, long, narrow cylindrical rotors make sample exchange difficult, since the exchange tube must be fabricated in such a way to direct the rotor from the magic angle through a bend up to a vertical tube [39]. A solenoid coil commonly used to provide radiofrequency (RF) power for the cylindrical rotor also has drawbacks with regards to perpendicular microwave coupling for dynamic nuclear polarization (DNP) [40–42].

We recently described a novel MAS apparatus utilizing a spherical rotor instead of a cylindrical rotor [43]. In our first paper, we showed that MAS spheres require only a single gas stream to provide friction-reducing bearing gas, drive propulsion to maintain spinning, and variable temperature control. Further, we demon-

* Corresponding author.
E-mail address: barnesab@wustl.edu (A.B. Barnes).

https://doi.org/10.1016/j.jmr.2019.03.006
1090-7807/

strated that spherical rotors spin stably about the spinning axis. Sample exchange was accomplished through direct access from the top of the magnet. However, in our first implementation of MAS spheres, a split solenoid coil was used to allow sample exchange and microwave coupling, which presented substantial disadvantages with regards to radio frequency performance.

Here we present a further development of MAS spheres. We scale the spherical rotors down to 4 mm to attain higher spinning frequencies and replace the split solenoid coil with a double-saddle coil to enhance RF homogeneity and the filling factor [44,45]. We report the first MAS cross polarization (CP) experiment on [U-^{13}C, ^{15}N] alanine spinning at 11.4 kHz using 4 mm spherical rotors. Spinning with helium gas provides access to spinning frequencies >28 kHz. Further, the stator design has been modified to fit a smaller coil and improve fiber optic detection for MAS frequencies. Lastly we examine the microwave coupling capability of 4 mm spheres through simulations of the microwave field distribution.

2. Materials and methods

High precision spheres are readily accessed through industrial sources (Ortech Advanced Ceramics, Sacramento, CA). In this current study, we further develop the use of Yttria stabilized ZrO_2 spheres for MAS, yet we emphasize that future studies will explore the use of other materials for spherical rotors such as CVD-diamond, Silicon Nitride, and polymers (plastics). A cylindrical sample chamber and six longitudinal turbine grooves on spheres (Fig. 1B and C) were machined by O'Keefe Ceramics (Woodland Park, CO). Note, the cylindrical sample chamber can only hold 3–4 μl of sample in 4 mm spheres, thus leading to a lower filling factor compared to the 4 mm cylindrical rotors. As we have demonstrated previously [43], the sample chamber can be further hollowed out to yield much improved filling factors and sensitivity. Three timing marks were laser printed between turbine grooves to measure the spinning frequency (Fig. 1C).

The spinning axis is first achieved using the turbine grooves of the sphere. The grooves on the sphere catch the high-velocity gas exiting the single aperture in the stator, leading to spinning along an axis parallel to the grooves. The grooves establish a rotation axis along the sample chamber, and the mass distribution of high-density zirconia contributes to a stable spinning axis. Once the spinning axis about the magic angle is established, conservation of the considerable angular momentum locks the rotor into a stable spinning axis. Due to the simultaneous bearing and turbine functions of spherical stator design implemented herein, the minimum stable spinning frequency of spherical rotors is higher than cylindrical rotors utilizing split drive and bearing pressures.

We machined 1.3 mm o.d. plug-cylinders (brown in Fig. 1C and D) from Vespel to seal the sample chamber. A gradual slope to the o.d. was machined to provide a very tight fit of the plug, and the plugs were inserted using liquid nitrogen. After inserting the plugs, the protruding surfaces were cut and sanded down to achieve a smooth surface. In this way, the spheres are sealed tight enough to prevent leakage of liquids, even at high spinning frequencies. The plug-cylinders are one-use, and require machining to remove the plugs and access the sample.

Stators housing the spherical rotor were 3D printed from acrylonitrile-butadiene-styrene (Form2 SLA printer, Clear V4 Resin, Formlabs, Somerville, MA). The double-saddle coil was wrapped, by hand, around a 4.8 mm metal rod to set the inner diameter. The coil wire was 24 AWG polyurethane/nylon-coated copper magnet wire (Belden, St. Louis, MO), and Teflon tape was wrapped around the wire before forming the double-saddle coil geometry. Then coil leads were covered with corona dope (GC Electronics, Rockford, IL; black in the right of Fig. 1D). Experiments without Teflon tape and corona dope exhibited arcing with high-power proton decoupling fields.

All experiments were performed at B_0 = 7.05 T on a custom-built, two-channel transmission line probe [46]. The Larmor frequencies for ^{1}H and ^{13}C were 300.197 MHz and 75.491 MHz, respectively. A spherical rotor packed with 80% H_2O and 20% D_2O was used for shimming. Magic angle adjustment was carried out using ^{79}Br resonance of KBr powder within a spherical rotor. The CP spectrum was recorded with a rotor-synchronized, echo-detected CPMAS sequence. 896 scans were acquired and delay between scans is 3 s. Linewidths were obtained with DMfit [47]. The nutation frequency of the ^{13}C refocusing pulse during the echo was 64 kHz, while a nutation frequency of 78 kHz was used for both $\pi/2$ pulse and two-pulse phase modulation (TPPM) decoupling on ^{1}H [48]. Spinning frequencies were measured either with fiber optics and a MAS control unit (TecMag Inc., Houston, TX) for experiments within the magnet, or with a TL-880 laser tachometer (Terahertz Technologies Inc., Oriskany, NY) outside the magnet. In the low temperature experiments, helium gas was cooled by flowing it through a copper tube immersed in liquid nitrogen. Temperature was measured with a fiber optic temperature sensor (Neoptix Inc., Canada) placed adjacent to the spinning sphere.

3. Results and discussion

3.1. Stators and NMR probe

Four millimeter spherical rotors, and the supporting stators, were designed based on our previously reported 9.5 mm sphere apparatus [43]. Similar to stators for 9.5 mm spheres, the stators supporting 4 mm spherical rotors introduce a single gas stream 35.3° off B_0 to suspend the sphere and drive sample rotation at the magic angle of 54.7° (Fig. 1G) [43]. We have improved on the original stator design by including a tapered gas inlet in order to release the back pressure generated by the 0.6 mm diameter spinning gas aperture (Fig. 1A, E, F and G). In addition, the gas inlet to the stator now takes a curved trajectory, in order to center the sample with the magic angle adjust pivot. In this way, the sphere's position with respect to the static magnetic field, microwave irradiation, and sample exchange tube is impervious to magic angle adjustment. We also substantially increased the filling factor of the sample coil in this design by reducing the wall thickness around the hemispherical cup of stator, to accommodate a much smaller coil (Fig. 1B). Other aspects of this design are similiar to the stators for 9.5 mm spheres. More detail can be found in our first MAS sphere paper [43]. All together, we fabricated over 300 stators to implement and test the improvements outlined above. A major advantage of spherical rotors is the ability to quickly 3D print many stator designs for rapid prototyping for a fraction of the cost associated with stators that house cylindrical rotors.

For improved spinning frequency detection, two blind holes for fiber optics were introduced into the bottom of the stator and oriented towards the equator of the sphere (Fig. 1F and G). Note, the blind holes permit optical penetration though the very thin ends of the guide-holes, while also providing a stop to prevent the fiber optics from touching the spherical rotor directly. These two holes formed a 30° incident and reflected angle on the sphere surface for red laser detection.

In a major improvement of the four-turn split solenoid coil previously used for MAS spheres [43], here we implement a double-saddle coil for RF excitation and detection (Fig. 1A, B and D) [49]. This design still permits direct sample exchange through vertical access to the sphere, and also substantially improves RF performance. A two-channel transmission line probe provides a maximum nutation frequency of 110 kHz on ^{13}C with 820 W input

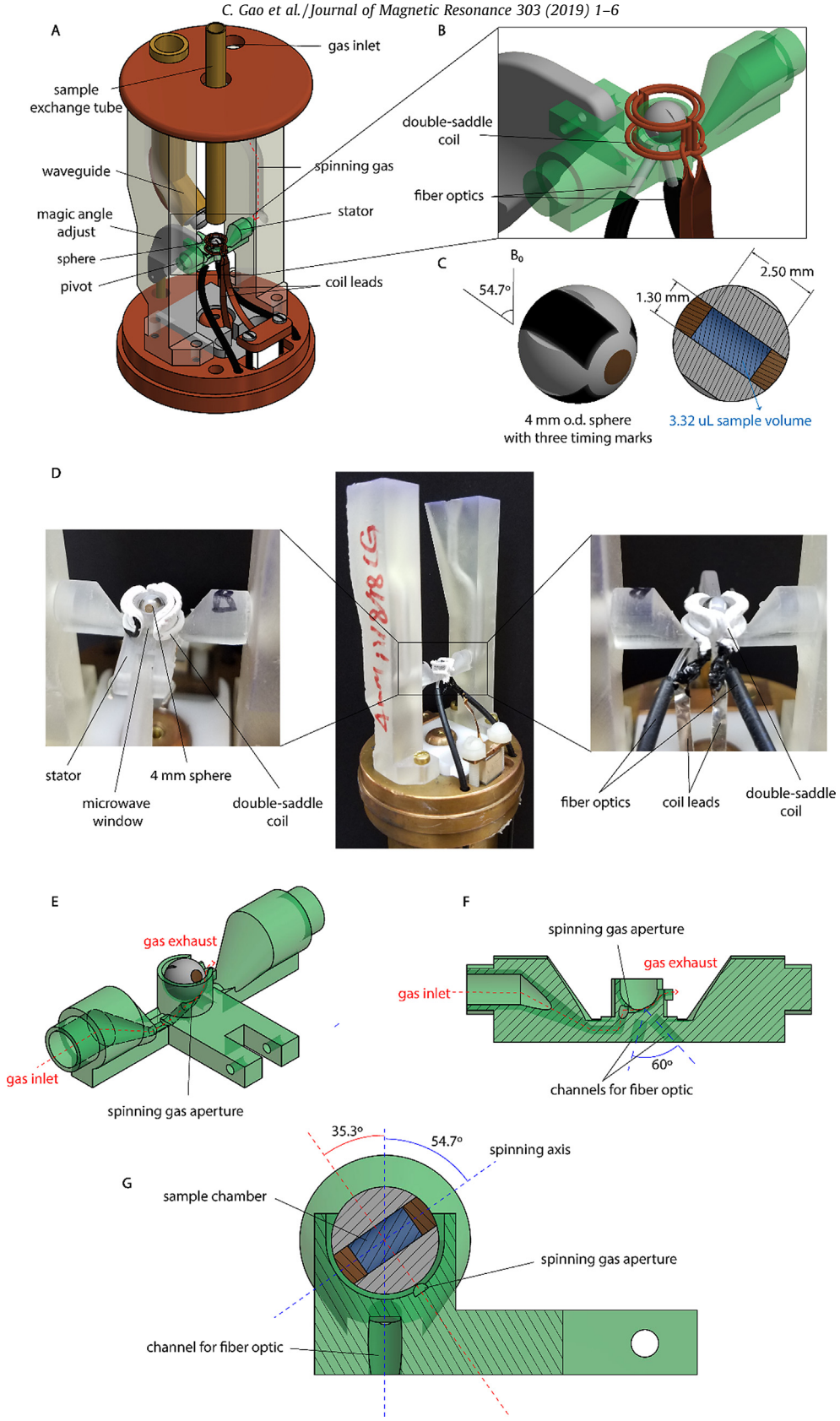

Fig. 1. Probe head accommodating a 4 mm spherical rotor. (A) Engineering schematics of the probe head, including the 4 mm o.d. spherical rotor, stator housing, fiber optics for spinning detection, double-saddle coil, magic angle adjustment assembly, waveguide and Teflon lens for DNP, tube for sample exchange, and 3D printed post for connection of the stator to the gas supply. (B) Expansion view of the 4 mm sphere and stator with double-saddle coil and fiber optics. (C) 4 mm o.d. spherical rotors with Vespel cylindrical plugs to seal the sample chamber. (D) Photographs of the probe head. The split in the double-saddle coil (shown on the left) serves as a window for microwave transmission. The waveguide and sample exchange tube have been removed for clarity. The double-saddle coil is wrapped with Teflon tape to prevent arcing at high decoupling power during TPPM. (E) Stator with spherical rotor oriented at the magic angle. Gas flow is indicated with a red dashed line. (F) A section view of E. Gas flow is indicated with a red dashed line. Fiber optics form an angle of 60° and point toward the sphere's equator. (G) A section view of E. The aperture for spinning gas at 35.3° off the magnetic field yields a spinning axis of 54.7°. (For interpretation of the references to color in this figure legend, the reader is referred to the web version of this article.)

power and 100 kHz on ^{1}H with 800 W input power [46]. Isolation was −42 dB from the ^{1}H to ^{13}C channel and −65 dB from the ^{13}C to ^{1}H channel, achieved with current nodes, series RC filters, and frequency selective RF traps [46]. Fig. 1D highlights the gap in the double-saddle coil, which creates a window for microwave transmission and additionally permits the optimal geometry for RF homogeneity [44,45].

3.2. CPMAS experiment with [U-^{13}C, ^{15}N] alanine

To evaluate the performance of 4 mm MAS spheres with double-saddle coil inductors, CPMAS experiments were conducted on [U-^{13}C, ^{15}N] alanine at room temperature (Fig. 2A). The nonregulated spinning frequency of 11.4 kHz using nitrogen gas was recorded with fiber optic detection (Fig. 2B). Maximum spinning frequencies were observed around 13 kHz using air for 4 mm spherical rotors. Although we have previously demonstrated regulated spinning stability of ±1 Hz of spherical rotors, here we show the unregulated spinning frequency as this data is a better indicator of the spinning stability achieved with rotors of varying geometry. Also, we note that the instability of the spinning frequency shown in Fig. 2B is most likely dominated by noise related to detection of the spinning, rather than true spinning instability. Using 78 kHz ^{1}H TPPM decoupling over 20 ms acquisition, linewidths of 152 Hz, 247 Hz, and 146 Hz were obtained for CO, C_α, and C_β, respectively. No obvious sidebands were observed due to the high spinning frequency.

The RF homogeneity of the double-saddle coil was analyzed through a ^{1}H nutation experiment using a Bloch decay pulse sequence on a sample of 80% H_2O and 20% D_2O within the 4 mm sphere. The ^{1}H RF homogeneity indicator calculated using the intensity ratio for an 810° pulse compared to a 90° pulse was 0.84.

In preparation for DNP experiments at cryogenic temperatures with high spinning frequencies, we examined spinning outside the magnet using low-temperature helium gas. Helium gas was cooled by flowing it through a copper tube immersed in liquid nitrogen bath. Fig. 2C shows the initial result of nonregulated spinning frequency >28 kHz at −60 °C.

3.3. Microwave simulations for DNP

We used High Frequency Structural Simulator (HFSS; Ansys, Canonsburg, PA) to investigate the efficiency of microwave transmission at 198 GHz into the 4 mm spherical rotors through the double-saddle coil. HFSS solves the Maxwell equations and simulates the propagation and focusing of millimeter waves in a time-dependent fashion [40,41,50]. The time-independent $\gamma_s B_{1s}$ of electron spins is then calculated using the same method as described previously [40,41,50].

The microwave input in the simulation is modeled as a pure Gaussian beam with a waist of 3.175 mm and a power of 5.0 W

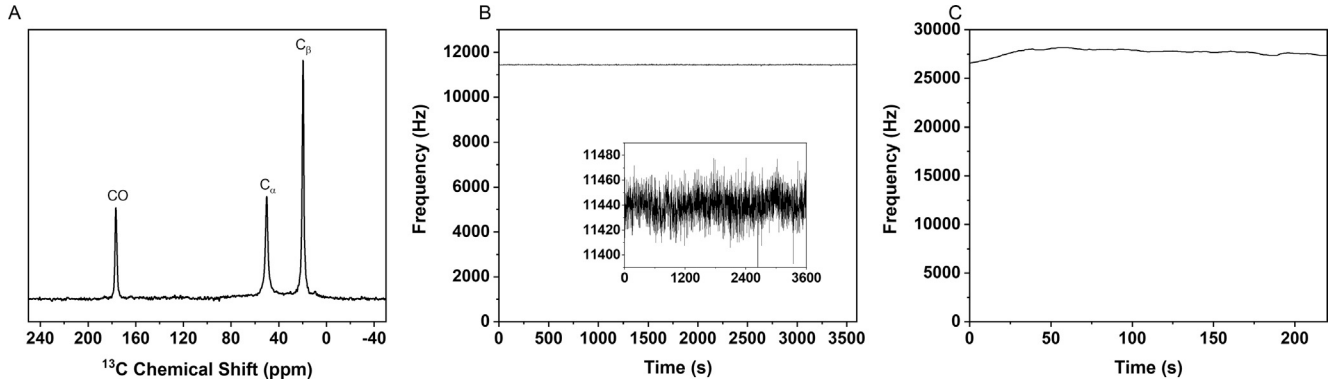

Fig. 2. NMR performance of the 4 mm spherical rotor with double-saddle coil. (A) CPMAS spectrum of [U-^{13}C, ^{15}N] alanine with spinning frequency of 11.4 kHz using nitrogen gas at ~45 psi. C_β, C_α, and CO peaks are observed at 19.6, 50.1, and 176.6 ppm, respectively. (B) Nonregulated spinning frequency of the 4 mm spherical rotor during CPMAS experiments recorded by fiber optic detection. (C) Nonregulated spinning frequency of 4 mm spherical rotor recorded with tachometer outside the magnet. A maximum spinning frequency of >28 kHz was achieved with helium gas (~110 psi) at −60 °C.

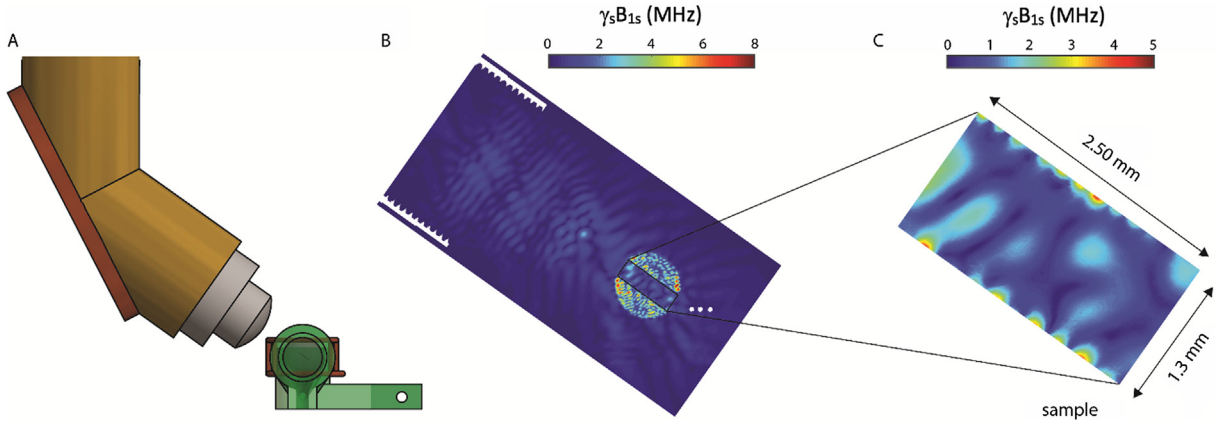

Fig. 3. Electromagnetic simulation of microwave irradiation into a 4 mm spherical rotor. (A) Schematics of the waveguide, Teflon lens, double saddle coil, stator, and 4 mm spherical rotor. (B) Microwave analysis with geometry shown in A. (C) Microwave analysis of sample area in B.

[41,51]. In the simulation, the geometry is included within an air box with radiation boundary, assuming microwaves radiating out of the geometry are lost to its surroundings. The sample in the simulation is a 3.32 μL frozen water-glycerol matrix with a dielectric constant of 3.5 (ε_r) and a loss tangent of 0.007 ($\tan\delta = \varepsilon_i/\varepsilon_r$) [41,50]. The simulation included a Teflon lens within the waveguide to focus microwaves into the 4 mm spherical rotors (Fig. 3A and B). The stator housing the sphere, copper double-saddle coil, two Vespel plugs, and the water-glycerol sample were also included in the simulation (Fig. 3A). Although the maximum intensities appear within the zirconia sphere, the simulation shows an average $\gamma_s B_{1s}$ of 0.99 MHz over the sample area (Fig. 3C), which is almost 3-fold higher than calculated previously with 3.2 mm cylindrical rotors [40]. This is a promising result for implementation of DNP on 4 mm spherical rotors with a double-saddle coil.

4. Conclusions and outlook

With improvements to the apparatus for MAS spherical rotors, we demonstrate the first CPMAS experiment on spheres. Implementation of a double-saddle coil resulted in acceptable RF homogeneity and NMR Rabi frequencies, while maintaining sample exchange and improving microwave coupling capability. Scaling the spherical rotors to 4 mm o.d., we achieved a spinning frequency of >28 kHz at −60 °C using helium gas. Although 4 mm o.d. cylindrical rotor assemblies which include two drive tips manufactured by Doty Scientific can spin up to 24 kHz, typical 4 mm cylindrical rotors are limited to a maximum frequency of 15 kHz. We note that this is the first demonstration of 4 mm spherical rotors, and there are still considerable improvements to be made with respect to the turbine surface and propulsion of spherical rotors. Spherical rotors can be reinforced to be much thicker, specifically at the apex of mechanical stress from centrifugal forces. Therefore, they can access higher spinning frequencies than their cylindrical counterparts. We expect to reach spinning frequencies of >200 kHz with smaller spheres. Furthermore, our demonstration of spinning spheres at −60 °C, as well as microwave simulations, suggest a feasible path towards high performance DNP employing spherical rotors.

Acknowledgements

Funding: This research was supported by a NIH Director's New Innovator Award [grant number DP2GM119131], an NSF CAREER Award [grant number DBI-1553577], and a Camille Dreyfus teacher-scholar award. We thank Rachel Martin, Jessica Kelz, Jan Korvink and Robert Griffin for helpful discussions.

Competing interests

A.B.B. is an author on provisional patents related to this work filed by Washington University in Saint Louis (62/703,278 filed on 25 July 2018 and 62/672,840 filed on 17 May 2018). The authors declare no other competing interests.

References

[1] I.J. Lowe, Free induction decays of rotating solids, Phys. Rev. Lett. 2 (1959) 285–287, https://doi.org/10.1103/PhysRevLett. 2.285.
[2] E.R. Andrew, A. Bradbury, R.G. Eades, Nuclear magnetic resonance spectra from a crystal rotated at high speed, Nature. 182 (1958) 1659.
[3] J. Herzfeld, A.E. Berger, J. Herzfeld, A.E. Berger, Sideband intensities in NMR spectra of samples spinning at the magic angle, J. Chem. Phys. 6021 (2008), https://doi.org/10.1063/1.440136.
[4] J. Schaefer, E.O. Stejskal, Carbon-13 nuclear magnetic resonance of polymers spinning at the magic angle, J. Am. Chem. Soc. 1031 (1975) 1031–1032, https://doi.org/10.1021/ja00420a036.
[5] F.D. Doty, P.D. Ellis, Design of high speed cylindrical NMR sample spinners, Rev. Sci. Instrum. 52 (1981) 1868–1875, https://doi.org/10.1063/1.1136530.
[6] F.D. Doty, Solid state probe design, Encycl. NMR (2000) 4475–4484.
[7] F. Castellani, B. van Rossum, A. Diehl, M. Schubert, K. Rehbein, H. Oschkinat, Structure of a protein determined by solid-state magic-angle-spinning NMR spectroscopy, Nature 420 (2002) 98–102.
[8] I. Bertini, A. Bhaumik, R.G. Griffin, M. Lelli, R. Lewandowski, C. Luchinat, High-resolution solid-state NMR structure of a 17.6 kDa Protein, J. Am. Chem. Soc. 132 (2010) 1032–1040.
[9] M. Huber, S. Hiller, P. Schanda, M. Ernst, A. Bçckmann, R. Verel, A proton-detected 4D solid-state NMR experiment for protein structure determination, J. Phys. Chem. Chem. Phys. (2011) 915–918, https://doi.org/10.1002/cphc.201100062.
[10] R. Linser, B. Bardiaux, V. Higman, U. Fink, B. Reif, Structure calculation from unambiguous long-range amide and methyl 1H-1H distance restraints for a microcrystalline protein with MAS solid-state NMR spectroscopy, J. Am. Chem. Soc. (2011) 5905–5912, https://doi.org/10.1021/ja110222h.
[11] M.J. Knight, A.J. Pell, I. Bertini, I.C. Felli, L. Gonnelli, R. Pierattelli, Structure and backbone dynamics of a microcrystalline metalloprotein by solid-state NMR, Proc. Natl. Acad. Sci. U. S. A. 109 (2012) 11095–11100, https://doi.org/10.1073/pnas.1204515109.
[12] J.S. Retel, A.J. Nieuwkoop, M. Hiller, V.A. Higman, E. Barbet-Massin, J. Stanek, L. B. Andreas, W.T. Franks, B.J. Van Rossum, K.R. Vinothkumar, L. Handel, G.G. De Palma, B. Bardiaux, G. Pintacuda, L. Emsley, W. Kühlbrandt, H. Oschkinat, Structure of outer membrane protein G in lipid bilayers, Nat. Commun. 8 (2017) 1–10, https://doi.org/10.1038/s41467-017-02228-2.
[13] M.T. Eddy, L. Andreas, O. Teijido, Y. Su, L. Clark, S.Y. Noskov, G. Wagner, T.K. Rostovtseva, R.G. Griffin, Magic angle spinning nuclear magnetic resonance characterization of voltage-dependent anion channel gating in two-dimensional lipid crystalline bilayers, Biochemistry. 54 (2015) 994–1005, https://doi.org/10.1021/bi501260r.
[14] Q.Z. Ni, T.V. Can, E. Daviso, M. Belenky, R.G. Griffin, J. Herzfeld, Primary transfer step in the light-driven ion pump bacteriorhodopsin: an irreversible U-turn revealed by dynamic nuclear polarization-enhanced magic angle spinning NMR, J. Am. Chem. Soc. 140 (2018) 4085–4091, https://doi.org/10.1021/jacs.8b00022.
[15] A. McDermott, Structure and dynamics of membrane proteins by magic angle spinning solid-state NMR, Annu. Rev. Biophys. 38 (2009) 385–403, https://doi.org/10.1146/annurev.biophys.050708.133719.
[16] H. Yang, D. Staveness, S.M. Ryckbosch, A.D. Axtman, B.A. Loy, A.B. Barnes, V.S. Pande, J. Schaefer, P.A. Wender, L. Cegelski, REDOR NMR reveals multiple conformers for a protein kinase c ligand in a membrane environment, ACS Cent. Sci. 4 (2018) 89–96, https://doi.org/10.1021/acscentsci.7b00475.
[17] L.A. Baker, T. Sinnige, P. Schellenberger, J. de Keyzer, C.A. Siebert, A.J.M. Driessen, M. Baldus, K. Grünewald, Combined ^{1}H-detected solid-state NMR spectroscopy and electron cryotomography to study membrane proteins across resolutions in native environments, Structure 26 (2018) 161–170.e3, https://doi.org/10.1016/j.str.2017.11.011.
[18] M. Renault, S. Pawsey, M.P. Bos, E.J. Koers, D. Nand, R. Tommassen-, V. Boxtel, M. Rosay, J. Tommassen, W.E. Maas, M. Baldus, Solid-state NMR spectroscopy on cellular preparations enhanced by dynamic nuclear polarization, Angew. Commun. 51 (2012) 2998–3001, https://doi.org/10.1002/anie.201105984.
[19] M. Kaplan, A. Cukkemane, G.C.P. van Zundert, S. Narasimhan, M. Daniëls, D. Mance, G. Waksman, A.M.J.J. Bonvin, R. Fronzes, G.E. Folkers, M. Baldus, Probing a cell-embedded megadalton protein complex by DNP-supported solid-state NMR, Nat. Methods 12 (2015) 5–9, https://doi.org/10.1038/nmeth.3406.
[20] S.H. Park, B.B. Das, F. Casagrande, Y. Tian, H.J. Nothnagel, M. Chu, H. Kiefer, K. Maier, A.A. De Angelis, F.M. Marassi, S.J. Opella, Structure of the chemokine receptor CXCR1 in phospholipid bilayers, Nature 491 (2012) 779–783, https://doi.org/10.1038/nature11580.
[21] S.A. Shahid, B. Bardiaux, W.T. Franks, L. Krabben, M. Habeck, B. Van Rossum, D. Linke, Membrane-protein structure determination by solid-state NMR spectroscopy of microcrystals, Nat. Methods 9 (2012) 1212–1217, https://doi.org/10.1038/NMETH.2248.
[22] S. Wang, R.A. Munro, L. Shi, I. Kawamura, T. Okitsu, A. Wada, S. Kim, K. Jung, L.S. Brown, V. Ladizhansky, Solid-state NMR spectroscopy structure determination of a lipid-embedded heptahelical membrane protein, Nat. Methods 10 (2013) 1007, https://doi.org/10.1038/nmeth.2635.
[23] A.B. Siemer, C. Ritter, M. Ernst, R. Riek, B.H. Meier, High-resolution solid-state NMR spectroscopy of the prion protein HET-s in its amyloid conformation, Angew. Chem. – Int. Ed. 44 (2005) 2441–2444, https://doi.org/10.1002/anie.200462952.
[24] C.L. Hoop, H.-K. Lin, K. Kar, G. Magyarfalvi, J.M. Lamley, J.C. Boatz, A. Mandal, J. R. Lewandowski, R. Wetzel, P.C.A. van der Wel, Huntingtin exon 1 fibrils feature an interdigitated β-hairpin–based polyglutamine core, Proc. Natl. Acad. Sci. 113 (2016) 1546–1551, https://doi.org/10.1073/pnas.1521933113.
[25] T. Theint, P.S. Nadaud, D. Aucoin, J.J. Helmus, S.P. Pondaven, K. Surewicz, W.K. Surewicz, C.P. Jaroniec, Species-dependent structural polymorphism of Y145Stop prion protein amyloid revealed by solid-state NMR spectroscopy, Nat. Commun. 8 (2017), https://doi.org/10.1038/s41467-017-00794-z.
[26] A.T. Petkova, R.D. Leapman, Z.H. Guo, W.M. Yau, M.P. Mattson, R. Tycko, Self-propagating, molecular-level polymorphism in Alzheimer's beta-amyloid fibrils, Science 307 (2005) 262–265.
[27] G. Tong, Y. Pan, H. Dong, R. Pryor, G.E. Wilson, J. Schaefer, Structure and dynamics of pentaglycyl bridges in the cell walls of staphylococcus aureus by

13 C - 15 N REDOR NMR, Biochemistry 2960 (1997) 9859–9866, https://doi.org/10.1021/bi970495d.
[28] H. Takahashi, I. Ayala, M. Bardet, G. De Paëpe, J.-P. Simorre, S. Hediger, Solid-state NMR on bacterial cells: selective cell wall signal enhancement and resolution improvement using dynamic nuclear polarization, J. Am. Chem. Soc. 135 (2013) 5105–5110.
[29] C. Bougault, I. Ayala, W. Vollmer, J. Simorre, P. Schanda, Studying intact bacterial peptidoglycan by proton-detected NMR spectroscopy at 100 kHz MAS frequency, J. Struct. Biol. (2018), https://doi.org/10.1016/j.jsb.2018.07.009.
[30] L. Cegelski, S.J. Kim, A.W. Hing, D.R. Studelska, R.D.O. Connor, A.K. Mehta, J. Schaefer, Rotational-echo double resonance characterization of the effects of vancomycin on cell wall synthesis in staphylococcus aureus, Biochemistry (2002) 13053–13058, https://doi.org/10.1021/bi0202326.
[31] T. Wang, Y. Bum, M.A. Caporini, M. Rosay, L. Zhong, D.J. Cosgrove, Sensitivity-enhanced solid-state NMR detection of expansin' s target in plant cell walls, Proc. Natl. Acad. Sci. U. S. A. 110 (2013) 16444–16449, https://doi.org/10.1073/pnas.1316290110/-/DCSupplemental.
[32] L. Cegelski, R.D.O. Connor, D. Stueber, M. Singh, B. Poliks, J. Schaefer, Plant cell-wall cross-links by REDOR NMR Spectroscopy, J. Am. Chem. Soc. (2010) 16052–16057.
[33] J.A.H. Romaniuk, L. Cegelski, R. Way, L. Cegelski, Bacterial cell wall composition and the influence of antibiotics by cell-wall and whole-cell NMR, R. Soc. (2015) 370.
[34] A. Lesage, C. Gardiennet, A. Loquet, R. Verel, G. Pintacuda, L. Emsley, B.H. Meier, A. Böckmann, Polarization transfer over the water – protein interface in solids, Angew. Chem. 47 (2008) 5851–5854, https://doi.org/10.1002/anie.200801110.
[35] M. Etzkorn, A. Bo, A. Lange, M. Baldus, Probing molecular interfaces using 2D magic-angle-spinning NMR on protein mixtures with different uniform labeling, J. Am. Chem. Soc. 126 (2004) 14746–14751, https://doi.org/10.1021/ja0479181.
[36] S. Hayes, L. Van Wüllen, H. Eckert, W.R. Even, R.W. Crocker, Z. Zhang, Solid-state NMR strategies for the structural investigation of carbon-based anode materials, Chem. Mater. 9 (1997) 901–911, https://doi.org/10.1021/cm960389i.
[37] Z. Wang, N. Opembe, T. Kobayashi, N.C. Nelson, I.I. Slowing, M. Pruski, Quantitative atomic-scale structure characterization of ordered mesoporous carbon materials by solid state NMR, Carbon N. Y. 131 (2018) 102–110, https://doi.org/10.1016/j.carbon.2018.01.087.
[38] J. Trebosc, J.W. Wiench, S. Huh, V.S. Lin, M. Pruski, Studies of organically functionalized mesoporous silicas using heteronuclear solid-state correlation NMR spectroscopy under fast magic angle spinning, J. Ameican Chem. Soc. 127 (2005) 7587–7593, https://doi.org/10.1021/ja0509127.
[39] A.B. Barnes, M.L. Mak-Jurkauskas, Y. Matsuki, V.S. Bajaj, P.C.A. van der Wel, R. DeRocher, J. Bryant, J.R. Sirigiri, R.J. Temkin, J. Lugtenburg, J. Herzfeld, R.G. Griffin, Cryogenic sample exchange NMR probe for magic angle spinning dynamic nuclear polarization, J. Magn. Reson. 198 (2009) 261–270, https://doi.org/10.1016/j.jmr.2009.03.003.
[40] E.P. Saliba, E.L. Sesti, F.J. Scott, B.J. Albert, E.J. Choi, N. Alaniva, C. Gao, A.B. Barnes, Electron decoupling with dynamic nuclear polarization in rotating solids, J. Am. Chem. Soc. 139 (2017) 6310–6313, https://doi.org/10.1021/jacs.7b02714.
[41] D.E.M. Hoff, B.J. Albert, E.P. Saliba, F.J. Scott, E.J. Choi, M. Mardini, A.B. Barnes, Frequency swept microwaves for hyperfine decoupling and time domain dynamic nuclear polarization, Solid State Nucl. Magn. Reson. 72 (2015) 79–89, https://doi.org/10.1016/j.ssnmr.2015.10.001.
[42] T.V. Can, R.T. Weber, J.J. Walish, T.M. Swager, R.G. Griffin, Frequency-swept integrated solid effect, Angew. Chemie - Int. Ed. 56 (2017) 6744–6748, https://doi.org/10.1002/anie.201700032.
[43] P. Chen, B.J. Albert, C. Gao, N. Alaniva, L.E. Price, F.J. Scott, E.P. Saliba, E.L. Sesti, P.T. Judge, E.W. Fisher, A.B. Barnes, Magic angle spinning spheres, Sci. Adv. (2018) 1–8.
[44] F. Bonetto, E. Anoardo, M. Polello, Saddle coils for uniform static magnetic field generation in NMR experiments, Concepts Magn. Reson. Part B 29B (2006) 9–19, https://doi.org/10.1002/cmr.b.
[45] D.M. Ginsberg, M.J. Melchner, Optimum geometry of saddle shaped coils for generating a uniform magnetic field, Rev. Sci. Instrum. 41 (1970) 122, https://doi.org/10.1063/1.1684235.
[46] F.J. Scott, N. Alaniva, N.C. Golota, E.L. Sesti, E.P. Saliba, L.E. Price, B.J. Albert, P. Chen, R.D. O'Connor, A.B. Barnes, A versatile custom cryostat for dynamic nuclear polarization supports multiple cryogenic magic angle spinning transmission line probes, J. Magn. Reson. 297 (2018) 23–32, https://doi.org/10.1016/J.JMR.2018.10.002.
[47] D. Massiot, F. Fayon, M. Capron, I. King, S. Le Calvé, B. Alonso, J.O. Durand, B. Bujoli, Z. Gan, G. Hoatson, Modelling one- and two-dimensional solid-state NMR spectra, Magn. Reson. Chem. 40 (2002) 70–76, https://doi.org/10.1002/mrc.984.
[48] A.E. Bennett, C.M. Rienstra, M. Auger, K.V. Lakshmi, R.G. Griffin, A.E. Bennett, C. M. Rienstra, R.G. Griffin, Heteronuclear decoupling in rotating solids, J. Chem. Phys. 103 (1995) 6951–6958, https://doi.org/10.1063/1.470372.
[49] I.M. Litvak, C.A. Espinosa, R.A. Shapiro, A.N. Oldham, V.V. Duong, R.W. Martin, Pneumatic switched angle spinning NMR probe with capacitively coupled double saddle coil, J. Magn. Reson. 206 (2010) 183–189, https://doi.org/10.1016/j.jmr.2010.07.001.
[50] E.A. Nanni, A.B. Barnes, Y. Matsuki, P.P. Woskov, B. Corzilius, R.G. Griffin, R.J. Temkin, Microwave field distribution in a magic angle spinning dynamic nuclear polarization NMR probe, J. Magn. Reson. 210 (2011) 16–23, https://doi.org/10.1016/j.jmr.2011.02.001.
[51] F.J. Scott, E.P. Saliba, B.J. Albert, N. Alaniva, E.L. Sesti, C. Gao, N.C. Golota, E.J. Choi, A.P. Jagtap, J.J. Wittmann, M. Eckardt, W. Harneit, B. Corzilius, S.Th. Sigurdsson, A.B. Barnes, Frequency-agile gyrotron for electron decoupling and pulsed dynamic nuclear polarization, J. Magn. Reson. 289 (2018) 45–54, https://doi.org/10.1016/j.jmr.2018.02.010.